

WASHINGTON UNIVERSITY IN ST. LOUIS

The report for Washington University for the period follows.

ENGINEERING DEVELOPMENT OF SLURRY BUBBLE COLUMN REACTOR (SCBR) TECHNOLOGY

**Twenty-Fourth Quarterly Report
for
January 1 – March 31, 2001**

(Budget Year 6: October 1, 2000 – September 30, 2001)

**Chemical Reaction Engineering Laboratory (CREL)
Chemical Engineering Department
Washington University**

Objectives for the Sixth Budget Year

The main goal of this subcontract is to study the fluid dynamics of slurry bubble columns and address issues related to scaleup and design. The objectives set for the sixth budget year (October 1, 2000 – September 30, 2001) are listed below.

- Extension of CARPT database to high superficial gas velocity in bubble columns.
- Extension of the CARPT/CT database to gas-liquid-solid systems at high superficial gas velocity.
- Evaluation of the effect of sparger design on the fluid dynamics of bubble columns using the CARPT technique.
- Interpretation of LaPorte tracer data.
- Further improvement in Computational Fluid Dynamics (CFD) using CFDLIB and Fluent.

In this report, the research progress and achievements accomplished in the twenty-fourth quarter (January 1, 2001 – March 31, 2001) are summarized.

HIGHLIGHTS FOR THE 24th QUARTER

1. Three-Dimensional Dynamic Simulation of Bubble Columns

- Three-dimensional dynamic simulations of two-phase (air/water) transient flow in cylindrical bubble columns were performed using CFDLIB.
- The key dynamic features of bubble column flows -- consisting of a tornado-like upward spiral liquid motion, pushed by a high volume of gas that sweeps across the core region, and the downward liquid gulf stream within the wall region -- were captured by numerical simulation.
- The time-averaged liquid velocity vector plots compared well with the CARPT measurements of Degaleesan (1997).

2. Mean Axial Liquid Velocity Profiles – Numerical versus CARPT

- Three-dimensional dynamic simulations of two-phase (air/water) transient flow in cylindrical bubble columns were performed using CFDLIB. The simulations covered columns of three different diameters (6, 8 and 18 in.) operated at various superficial gas velocities (2 to 12 cm/s).
- The predicted overall gas holdup in each case was in good agreement with the experimentally measured value.
- The time-averaged radial profiles of the liquid axial velocity compared well with the CARPT data of Degaleesan (1997) in the 6- and 8-in. diameter column. However, there were discrepancies in the predicted inversion point and velocity profile shape for the 18-in. diameter column.

3. Evaluation of Turbulent Eddy Diffusivity in Bubble Columns by Numerical Particle Tracking

- Numerical liquid-phase particle tracking simulations were performed using CFDLIB. The simulations covered columns of two different sizes (8- and 18-in. diameters) operated at superficial gas velocities of 12 and 10 cm/s, respectively.
- The Lagrangian turbulent eddy diffusivity for the liquid phase was evaluated using the numerically tracked particle trajectories and compared with the corresponding values calculated from CARPT data.
- The numerically predicted axial diffusivities agreed well with the measured values; the agreement for the azimuthal diffusivities was less impressive, while the values for the radial diffusivities were significantly under-predicted.

1. Three-Dimensional Dynamic Simulation of Bubble Columns

1.1 Introduction

It is widely recognized that the physical models used in the current numerical investigations, which include the inter-phase momentum exchange models and multiphase turbulence models, require experimental data for verification and improvement. Three-dimensional dynamic simulations of the highly transient gas-liquid flow in either cylindrical or rectangular bubble columns are needed.

In this study we present a Eulerian/Eulerian dynamic simulation of a three-dimensional gas-liquid bubble column using the Los Alamos finite-volume multiphase flow simulation library, CFDLIB. We focus on the comparisons with the experiments of Degaleesan (1997), who studied the fluid dynamics of bubble columns by using the Computer Automated Radioactive Particle Tracking (CARPT) technique in our laboratory.

For the purpose of the present simulations, we have modified some parts of the code related to the inter-phase momentum exchange and turbulence calculations. For the drag coefficient, C_D , we use the following expression (Drew 1983):

$$C_D = \max \left[\frac{24}{Re} (1 + 0.15 Re^{0.687}), f \frac{8}{3} \frac{Eo}{Eo + 4} \right] \quad (1.1)$$

in which

$$f = \left\{ \frac{1 + 17.67(1 - \varepsilon)^{9/7}}{18.67(1 - \varepsilon)^{3/2}} \right\}^2 \quad (1.2)$$

The Eotvos number, Eo , and bubble Reynolds number, Re , are defined as

$$Eo \equiv E g \rho_c d_p^2 / \gamma \quad (1.3)$$

And

$$Re \equiv d_b |\mathbf{u}_l - \mathbf{u}_g| / \nu_l \quad (1.4)$$

In the momentum equation for the liquid phase, we adopted a model for the bubble-induced stress, as proposed by Sato *et al.* (1981):

$$\sigma_c^b = \rho_c \nu_b^t (\nabla \mathbf{u}_l + \nabla \mathbf{u}_l^T) \quad (1.5)$$

in which the bubble-induced additional viscosity is calculated by

$$\nu_b^t = k_b \varepsilon d_b |\mathbf{u}_l - \mathbf{u}_g| \quad (1.6)$$

The empirical constant k_b takes a value from 0.2 to 0.6, and is taken as 0.4 in this simulation.

1.2 Results and Discussion

All simulations start from a static initial condition where the main body of the column is filled with water and the top part only with gas. Figure 1.1 shows a typical mesh system

used for a cylindrical column. CFDLIB requires a structured mesh system consisting of logical cubic cells. At the cross-sectional plane (x - y plane), the elliptically smoothed, body-fitted mesh is used. In the axial direction (z -direction), the grid is uniform. In order to obtain a better comparison with experimental data, we set the conditions for our simulations as close to those in Degaleesan's (1997) experiment as possible. Initially the column is filled with liquid (water), i.e., $\varepsilon_l = 1$; $\varepsilon_g = 0$, up to the level that matches the static liquid height in the experiment. Above this level, the initial condition is $\varepsilon_l = 0$; $\varepsilon_g = 1$. To prevent liquid flooding from the column, the computational domain in the axial direction is about 50 to 80% higher than the static liquid height. The gas is introduced at the bottom of the column, and only gas is allowed to cross the bottom boundary. Since it is very difficult and not necessary to resolve the gas injectors used in the experiments (e.g., 0.5-1.0-mm-diameter holes on perforated plate) with the currently employed mesh, the gas is introduced uniformly over the bottom plane. For the gas phase, the free-slip boundary condition is imposed on the column's wall. For the liquid phase, since the thin boundary layer cannot be resolved, either the free-slip or the no-slip condition can be used. Finally, the pressure condition, i.e., the atmospheric pressure $p = 0$, is imposed on the top of the column.

The gas-liquid flow in bubble columns is highly transient and turbulent. Figure 1.2 shows the instantaneous iso-surfaces of the gas volume fraction in columns of different diameters operated at different superficial gas velocities. The plots show the three-dimensional spiral structures and transient pockets of high gas volume fraction mixtures rising up in a continuous fashion. Figure 1.3 shows the instantaneous contour plot of gas holdup on a central ($r - z$) plane of the 44-cm diameter column operated at 2, 5 and 10 cm/s superficial gas velocities. Here we see that the free surface, i.e., the dynamic height of the gas-liquid mixture in the column, rises as the superficial gas velocity increases. The turbulent character of the flow can be further observed by looking at the instantaneous velocity fields. Figure 1.4 shows the instantaneous liquid velocity vectors projected on a ($r - z$) plane (at $\theta = 0$) of the 44-cm diameter column. One can clearly see the spiral structures associated with the transient eddies. Figure 1.5 shows the snapshots of liquid velocity vectors on cross-sectional ($x - y$) planes located at the top, middle and bottom regions of the column. The vortices are observed in the middle and bottom sections. At the upper end of the column, the gas disengagement zone, as shown in Figure 1.5(a), resembles a fountain-like pattern. In Figure 1.6, we exhibit the correlation between liquid velocity and gas holdup. Figure 1.6(a) is the top view of the instantaneous liquid velocity vector (3D) plot, on a cross-sectional plane located at the middle section, overlapped by the gas holdup contour plot on the same plane. The flow visualization package used does not allow the display of negative velocities. We notice that the upward rising vortices ($u_z > 0$) are associated with the high gas holdup pockets, as indicated by the dark areas in Figure 1.6(a). By comparing Figure 1.6(a) with Figure 1.6(b), in which only the liquid velocity vectors are plotted, we see that all the vortices are accompanied by upwards motion, and the non-vortical areas are in downwards motion. Hence, as shown in Figures 1.2-1.6, our simulations reveal the dynamic features of bubble columns -- tornado-like upward spiral liquid motion pushed by a high volume of gas that sweeps across the core region and the downwards liquid gulf stream within the

wall region. It is such spiral motions that push the gas towards the center of the column, resulting in the non-uniform radial distribution of gas holdup. It should be noted that the visualizations shown in Figures 1.2-1.6 are chosen at random, in time and/or in space, from the simulations. Due to the turbulent/transient nature of the flows, the exact time and location of these plots are obviously not relevant to the qualitative observations.

Figure 1.7 shows the longitudinal sections (side view) of the time-averaged liquid velocity vector plots for the 14-cm diameter column. The angle between the longitudinal planes is $\pi/4$. The choice of these planes is arbitrary. Spanning the entire column, the single-cell circulation flow pattern is clearly seen from various side views, as observed experimentally by Devanathan (1991) and Degaleesan (1997). In addition, the flow pattern is reasonably symmetric with respect to the column axis. From a height of about one column diameter, D_c , above the distributor, the flow appears to be quite well developed, with negligible radial and angular velocities.

Figure 1.8 shows the cross-sectional views of the time-averaged liquid velocity vectors for the same cases shown in Figure 1.7. At the upper end of the column, near the disengagement zone, the flow reversal is symmetric about the column axis, as shown by the upper plot of Figure 1.8, resembling a fountain like pattern with negligible angular velocity component. In the middle section, both the radial and angular time-averaged velocity components are negligibly small. This indicates that time-averaged liquid velocity in the middle section of the column is nearly one-dimensional, i.e. unidirectional with radial dependency only. At the bottom of the column, shown by the lower plot of Figure 1.8, the inwards flow pattern is the result of liquid descending along the column wall. All of these cross-sectional views of the time-averaged liquid velocity vectors compare well with CARPT measurements (Degaleesan, 1997).

2. Mean Axial Liquid Velocity Profiles – Numerical versus CARPT

2.1 Introduction

We have completed the three-dimensional dynamic simulations for three sizes of bubble columns operated at different superficial gas velocities. The conditions used in the simulations were the same as those employed in the CARPT experiments performed in our laboratory. The diameters of the columns and the operating conditions, i.e., the superficial gas velocity, for each case are listed in Table 2.1. The cases studied cover flow regimes ranging from bubbly flow to churn turbulent flow. The objective was to validate the numerical results by comparison with data, and further, to assess the capacity of the current two-fluid model to predict the fluid dynamics in bubble column reactors. In the present report we focus on the comparison of the mean axial liquid velocity.

CFDLIB, a package developed by the Los Alamos National Laboratory, was used for the simulations presented in this report. The modifications of part of the code related to the inter-phase momentum exchange and turbulence calculations and the numerical mesh system employed for our simulation were discussed in the previous report (October – December 2000).

2.2 Results and Discussion

All simulations start from a static initial condition in which the main body of the column is filled with water and the top part only with gas. The simulations are then performed until a quasi-steady state is reached. The time-averaged quantities are then calculated. In all simulations, the velocity and gas holdup fields are sampled every 0.05 - 0.1 seconds. To ensure the convergence of the averaged quantities, the averaging processes are performed for 50 - 80 seconds. The spatial averaging is then conducted along the vertical direction within the lower, middle and upper sections of the column.

The grid size and boundary conditions used are listed in Table 2.1. For each simulation, we first compared the overall global gas holdup, indicated by a column's dynamic height, with the experimental measurements, as listed in Table 2.1. The dynamic heights from the simulations were obtained by time-averaging the fluctuating interface level. The agreement between calculated and measured overall gas holdup was excellent (within a couple of percentage points), except at the highest gas velocity in the smallest diameter column.

Figure 2.1 shows the time- and azimuthally averaged axial liquid velocity profiles, $U_z(r)$, for a 14-cm diameter column at different superficial gas velocities. Some results for the 14-cm diameter column simulation were reported before. The compared profiles concerned the middle section of the column, where the mean flow could be assumed to be one-dimensional. For this relatively small diameter column, the simulation results at high U_g (9.6 and 12 cm/s) were in better agreement with the data than those at lower U_g (2.4 and 4.8 cm/s).

Figure 2.2 compares the numerically predicted radial distribution of the mean axial liquid velocity with experimental data in a 19-cm diameter column operated at 2, 5 and 12 cm/s superficial gas velocity. For these three cases, the numerical predictions agreed quite well with the data. The effect of using a different boundary condition on the wall can be seen by comparing the curves of the cases with no-slip condition ($U_g=2$ and 5 cm/s) with that of the free-slip condition ($U_g=10$ cm/s). The free-slip condition yielded better agreement with data in the near-wall region than did the no-slip condition. Obviously the boundary layer is too thin to be resolved by either measurement or simulation. For the gas-driven flow as found in bubble columns, the wall boundary is of less interest. Further, the wall friction is negligible in the global momentum balance. For these reasons, we consider the free-slip wall boundary condition appropriate for the cases of realistic superficial gas velocity, say $U_g > 10$ cm/s.

Figure 2.3 compares the numerical mean velocity profiles with CARPT-measured profiles for the 44-cm diameter column operated at superficial gas velocities of 2, 5 and 10 cm/s. There are two noticeable differences between the calculated and the measured results. The inversion points, i.e., the radial location where $U_z=0$, for all the experimental profiles fall at $r/R \approx 0.68$, while those for the numerically predicted profiles move outwards to $r/R \approx 0.75$. This is an indication of the discrepancy in computed and actual

gas holdup profiles, i.e., the time-averaged radial distribution of gas holdup. We also notice that the experimental liquid velocity profiles for $U_g=5$ cm/s and 10 cm/s are fairly close. It seems that as U_g increases beyond a certain value, the liquid velocity does not linearly increase any more to the extent observed at lower U_g . Such behavior may indicate a transition from bubbly flow to churn turbulent flow where the mechanisms of bubble-bubble and bubble-liquid interactions are different. However, the model adopted in the current simulation is based on the assumption of single-size bubbles and neglects bubble-bubble interactions and therefore cannot account for such a change of mechanism. The possible transition, therefore, is not reflected in the numerical profiles shown in Figure 2.3. Further investigations of the reasons for the discrepancies between experimented and observed velocity profiles are in progress.

Table 1. Column Size, Operating Conditions and the Corresponding Computational Parameters

Column diameter D_c (cm)	Superficial gas velocity U_g (cm/s)	Static liquid height (cm)	Measured dynamic height (cm)	Measured overall gas holdup	Simulated dynamic height (cm)	Computed overall gas holdup	$\Delta x, \Delta y$ (cm)	Δz (cm)	Wall boundary condition
14	2.4	98	105	0.067	106	0.075	0.93	1.96	free-slip
	4.8	98	112	0.125	113	0.133	0.70	1.23	no-slip
	9.6	98	123	0.203	124	0.209	0.70	1.53	no-slip
	12	98	126	0.222	137	0.285	0.93	2.45	free-slip
19	2	104	115	0.093	110	0.054	1.1	2.1	no-slip
	5	104	128	0.191	123	0.154	1.1	2.1	no-slip
	12	96	124	0.230	130	0.262	1.1	1.9	free-slip
44	2	179	193	0.073	192	0.068	2.2	4.5	free-slip
	5	179	210	0.147	210	0.148	2.2	4.5	free-slip
	10	176	218	0.191	220	0.200	2.2	4.4	no-slip

3. Evaluation of Turbulent Eddy Diffusivity in Bubble Columns by Numerical Particle Tracking

3.1 Introduction

The dispersion of passive scalars by continuous motion in turbulent flows evolved as a major field of research, particularly during recent years. This evolution was due to industrial and environmental issues of utmost importance related to the energy crisis, spreading pollution and the need to improve plant design for two- or multi-phase flow processes. In the design of bubble column reactors, liquid phase mixing is one of the important factors that not only governs the residence time distribution of the liquid, but also affects that of the gas phase, and in addition, determines the mean driving force for mass transfer. As is well known, turbulence largely enhances the transport and mixing of any passive scalar released to a continuous material phase. The rates of transfer and mixing in the presence of turbulence are orders of magnitude larger than the rates due to molecular transport alone. The most common method of dealing with equations governing turbulent flow is treating the diffusive nature of turbulence via the introduction of a turbulent diffusivity for a given quantity. This is usually done using the gradient model, based on the well-known Boussinesq's hypothesis. With a suitable diffusivity, such a model appears in the averaged mass balance equation as a diffusive term. However, the turbulent eddy diffusivity that appears in the resulting equations is itself unknown and needs to be modeled.

While molecular diffusivity is caused by the Brownian motion of molecules, the turbulent eddy diffusivity is naturally related to the Lagrangian turbulent motion of fluid particles. Measurements and simulations of fluid particle velocities and trajectories, in a Lagrangian framework, are therefore needed for the study of the turbulent eddy diffusivity. The CARPT technique is capable of recording the Lagrangian trajectory of a tracer particle traveling through the entire column in a reasonable period of time. The Lagrangian turbulent eddy diffusivities are then directly evaluated from such data. Similarly, numerical particle tracking can be performed in a velocity field generated by the dynamic simulations of the transient gas-liquid flow in bubble columns. The numerical particle trajectories can then also be used to calculate the Lagrangian turbulent eddy diffusivities. In this sense there is no difference between the CARPT data and the data from numerical particle tracking.

However, there has been no generally established relationship between the eddy diffusivities, arising from the Boussinesq's gradient approximation, and the turbulent eddy diffusivities defined in the Lagrangian framework. In an isotropic and homogeneous turbulence field, it has been shown that the diffusivity appearing in the convection-diffusion equation can be approximated by the Lagrangian-based turbulent eddy diffusivities (Tenneke and Lumley, 1972). This is accomplished by using scale arguments and by comparing the probability distribution function for the spread of particles with the solution of the turbulent convective diffusion equation. Even without such a relation, the Lagrangian information deduced from a CARPT experiment directly reveals the characteristics of the dispersion process in the liquid phase and can be utilized

to study and model the effect of fluid dynamics on liquid-phase mixing in bubble columns.

In this report we evaluate the Lagrangian turbulent eddy diffusivity in bubble columns by utilizing numerical particle tracking. We compare the diffusivities from CARPT measurements with the ones from numerical simulation. Such comparison also serves as a validation of the numerical predictions arising from the two-fluid simulation of bubble column hydrodynamics.

3.2 Results and Discussion

As stated in the previous report (October – December 2000), we completed the three-dimensional dynamic simulations for bubble columns of three sizes operated at different superficial gas velocities and compared the time-averaged quantities with the data from CARPT experiments. From these simulations, we chose two cases for particle tracking simulation: a 44-cm diameter column operated at a superficial gas velocity of 10 cm/s and a 19-cm diameter column operated at $U_g=12$ cm/s. Both cases are within the churn turbulent flow regime, which is of interest to us. The simulations start from fully developed flow fields. Unlike the CARPT experiment, where the technique is able to follow a single tracer particle only, numerically there is no limit to the number of particles that can be traced simultaneously. Typically, 5000 initially randomly seeded particles are followed in a simulation. The dynamic simulation of the fluid flow field continues while the particle tracking is being performed. For the cases reported here, the simulation ran about 20 seconds, and the sampling frequency for the particle trajectory was 50 Hz, the same as in CARPT experiments, i.e., the position of the particle was recorded every 0.02 second. Figure 3.1 shows the trajectory of a numerical particle that was arbitrarily chosen from the 5000 particles, and the trajectory of the CARPT particle in the same column and under the same operating condition. The trajectory displayed represents 20 seconds from an arbitrary starting position.

For the general case, the turbulent eddy diffusivity is a second order tensor. In a Cartesian coordinate system, it is defined as

$$D_{ij}(\tau) \equiv \frac{1}{2} \frac{d}{d\tau} \overline{\{x_i(\tau+t) - x_i(t)\} \{x_j(\tau+t) - x_j(t)\}} \quad (3.1)$$

where the over bar indicates the averaging over time t and different particles. In terms of cylindrical coordinates, each component of the diffusivity tensor is calculated as

$$D_{rr} = \overline{u_x \Delta x \cos^2 \theta + u_y \Delta y \sin^2 \theta + \cos \theta \sin \theta (u_y \Delta x + u_x \Delta y)} \quad (3.2)$$

$$D_{\theta\theta} = \overline{u_x \Delta x \sin^2 \theta + u_y \Delta y \cos^2 \theta - \cos \theta \sin \theta (u_y \Delta x + u_x \Delta y)} \quad (3.3)$$

$$D_{zz} = \overline{u_z \Delta z} \quad (3.4)$$

$$D_{r\theta} = \overline{(u_x \Delta y + u_y \Delta x)(\cos^2 \theta - \sin^2 \theta)} + 2 \sin \theta \cos \theta \overline{(u_y \Delta y - u_x \Delta x)} \quad (3.5)$$

$$D_{rz} = \overline{(u_x \Delta z' + u_z' \Delta x) \cos \theta} + \overline{(u_y \Delta z' + u_z' \Delta y) \sin \theta} \quad (3.6)$$

$$D_{\theta z} = \overline{(u_y \Delta z' + u_z' \Delta y) \cos \theta} - \overline{(u_x \Delta z' + u_z' \Delta x) \sin \theta} \quad (3.7)$$

in which

$$\Delta x = x(\tau + t) - x(t); \quad \Delta y = y(\tau + t) - y(t); \quad \Delta z' = z'(\tau + t) - z'(t);$$

$$u_x = u_x(\tau + t); \quad u_y = u_y(\tau + t); \quad u_z' = u_z'(\tau + t)$$

$$\cos \theta = \frac{x(\tau + t)}{\sqrt{x^2(\tau + t) + y^2(\tau + t)}}; \quad \sin \theta = \frac{y(\tau + t)}{\sqrt{x^2(\tau + t) + y^2(\tau + t)}};$$

Here we need to exclude the effect of convection due the mean axial velocity, $U_z(r)$, by using

$$u_z'(\tau + t) = u_z(\tau + t) - U_z[r(t + \tau)]; \quad r = \sqrt{x^2(t + \tau) + y^2(t + \tau)}; \quad (3.8)$$

for the fluctuating velocity in axial direction and

$$z'(t) = \int_0^t u_z'(s) ds \quad (3.9)$$

for the displacement in axial direction caused by the above fluctuating velocity only.

Figure 3.2 compares the numerical values of D_{zz} , D_{rr} and $D_{\theta\theta}$ with those evaluated from CARPT data for the 44-cm-diameter column operated at a superficial gas velocity of 10 cm/s. Figure 3.3 shows the same comparison for the 19-cm-diameter column operated at a superficial gas velocity of 12 cm/s. For both cases, the numerical simulation predicted the axial diffusivity, D_{zz} , quite satisfactorily. However, the simulations under-predicted the peak values of the radial diffusivity, D_{rr} , by about 100%. Asymptotically, the numerical radial diffusivity approached zero, while the experimental radial diffusivity approached finite values. The reasons for this discrepancy will be studied in the future. The numerically predicted azimuthal diffusivities, $D_{\theta\theta}$, behaved similarly to the measured values. As stated earlier, one of the objectives of evaluating the Lagrangian turbulent eddy diffusivities is to determine whether these diffusivities are appropriate terms to use in the gradient diffusion model. From a practical point of view, most proposed models are either 1D or 2D, such as the axial dispersion model (ADM)

and the recycle and cross flow with dispersion (RCFD) model (Degaleesan, 1997). Only the radial and axial eddy diffusivities are therefore of interest. For an axial dispersion model, one needs the axial eddy diffusivity and the mean liquid velocity, i.e., the liquid re-circulation, profile to evaluate the dispersion coefficient, as shown by Degaleesan and Dudukovic (1998). We have shown here that the 3D dynamic simulations can provide such information with reasonable accuracy.

Future Work

Estimating the local interfacial area has been derived from the overall gas holdup estimate, assuming mean bubble size. Estimating this interfacial area provides one of the most important bubble column reactor modeling parameters. In a recent development, local interfacial area was calculated locally, based upon predicted local gas holdup and assumed mean bubble size in current CFD simulation.

In its next report, Washington University expects to introduce the bubble population balance equation that has been deemed necessary to the attainment of better and more accurate estimates.

References

- Degaleesan, S., "Fluid dynamic measurements and modeling of liquid mixing in bubble columns," D. Sc. Thesis, Washington University in St. Louis (1997).
- Degaleesan, S. and M. P. Dudukovic, "Liquid backmixing in bubble columns and the axial dispersion model," *AICHE J.*, **44**(11), 2369-2378 (1998).
- Devanathan, N., "Investigation of liquid hydrodynamics in bubble columns via computer automated radioactive particle tracking (CARPT)," D. Sc. Thesis, Washington University in St. Louis (1991).
- Drew, D. A., "Mathematical modeling of two-phase flow", *Ann. Rev. Fluid Mech.*, **15**, 261 (1983).
- Sato, Y., M. Sadatomi and K. Sekoguchi, "Momentum and heat transfer in two-phase bubble flow I," *Int. J. Multiphase Flow*, **7**, 167 (1981).
- Tennekes, H. and J. L. Lumley, "A first course in turbulence," The MIT Press, Cambridge, Massachusetts, USA (1972)

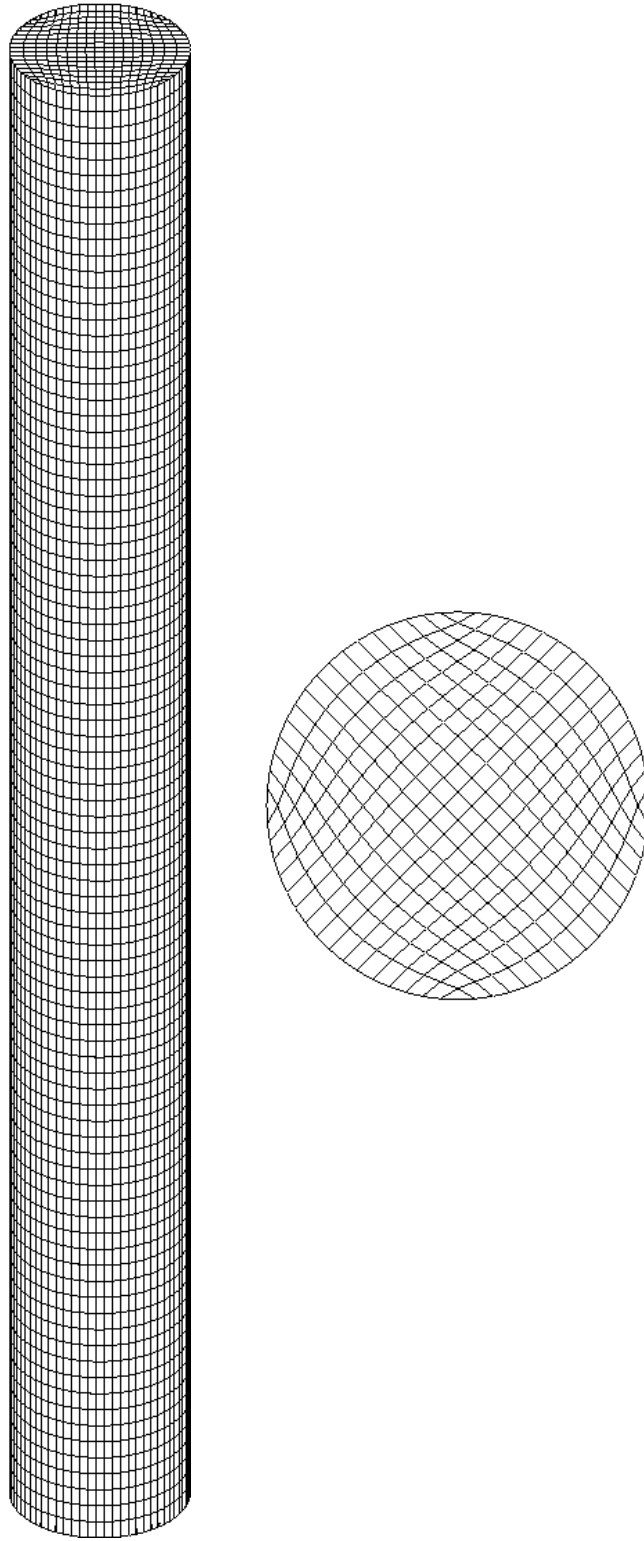


Figure 1.1 Computational Meshes

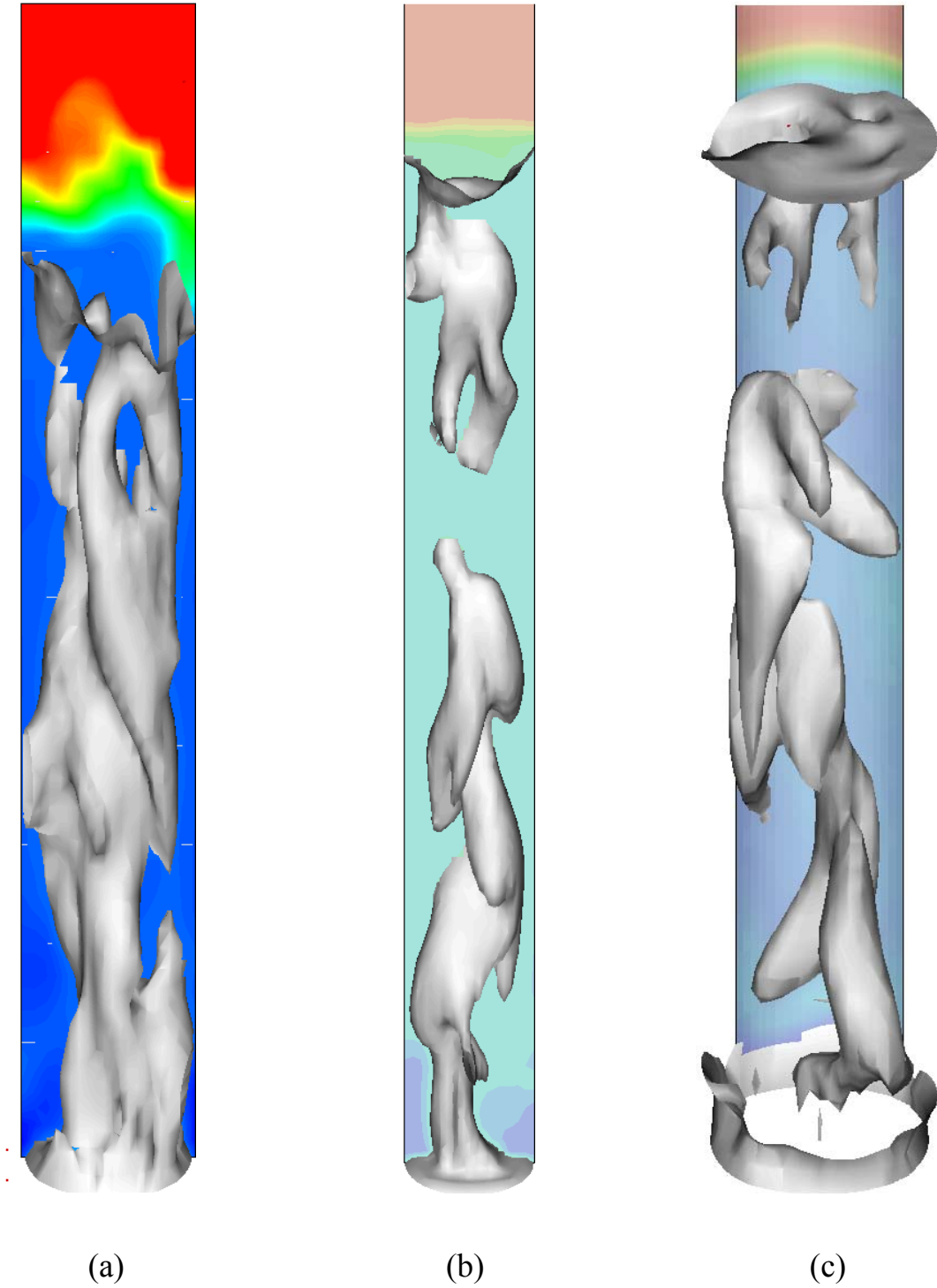
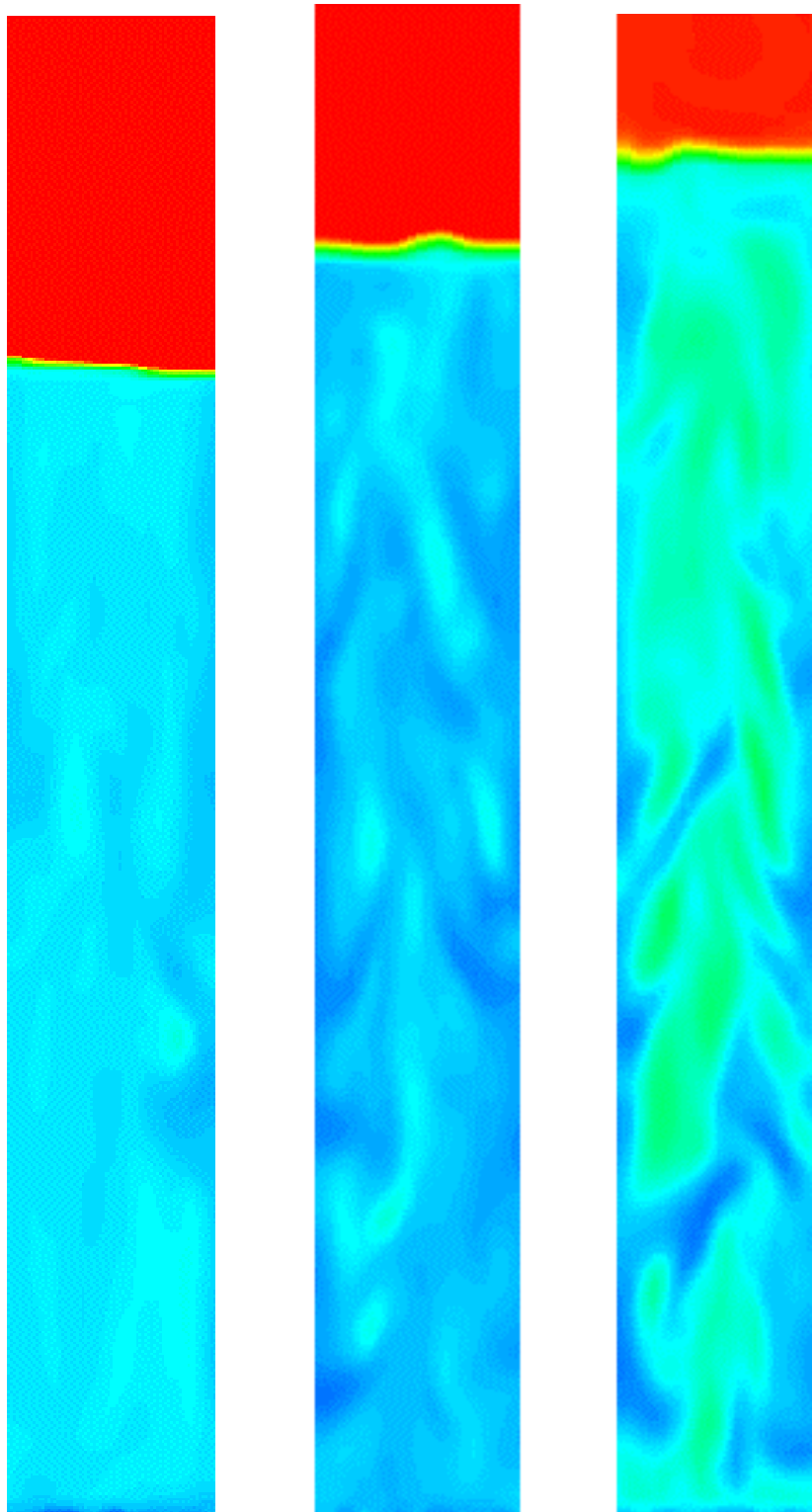


Figure 1.2 The Instantaneous Iso-Surface of the Gas Holdup, ϵ_g , in Various Bubble Columns: (a) $D_c = 19\text{cm}$; $U_g = 2\text{cm/s}$; $\epsilon_g = 0.08$ (b) $D_c = 14\text{cm}$; $U_g = 9.6\text{cm/s}$; $\epsilon_g = 0.33$ (c) $D_c = 44\text{cm}$; $U_g = 10\text{cm/s}$; $\epsilon_g = 0.28$

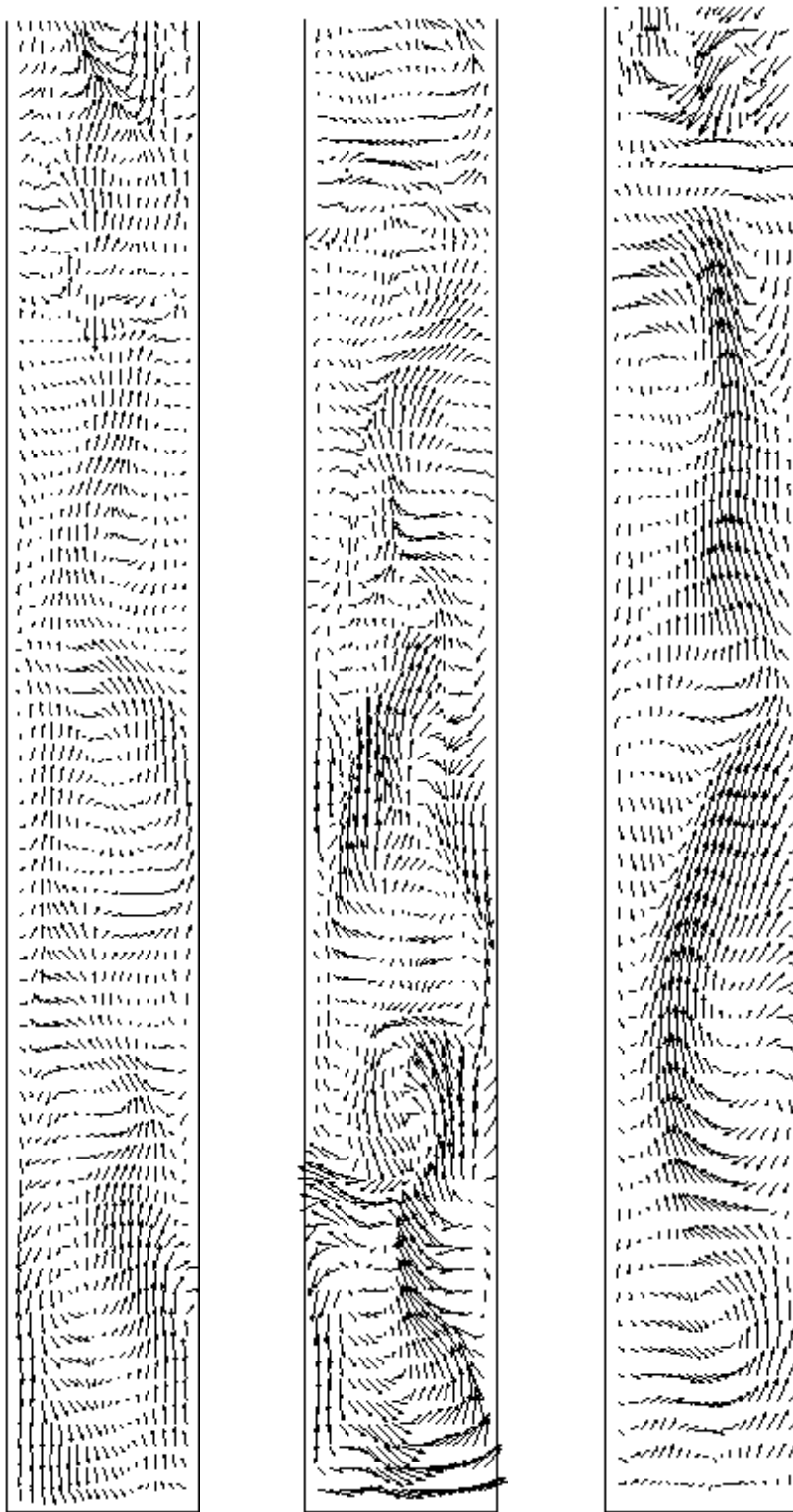


(1) 2cm/sec

(2) 5cm/sec

(3) 10cm/sec

Figure 1.3 Contour Plot of the Instantaneous Gas Holdup on a Plane Slice through the Center of a 44-cm Diameter Column Operated at Different Superficial Gas Velocities

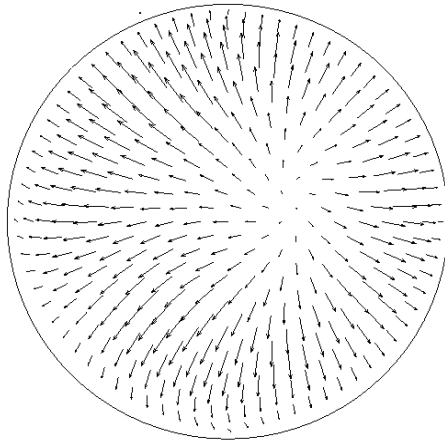


(1) 2 cm/s;

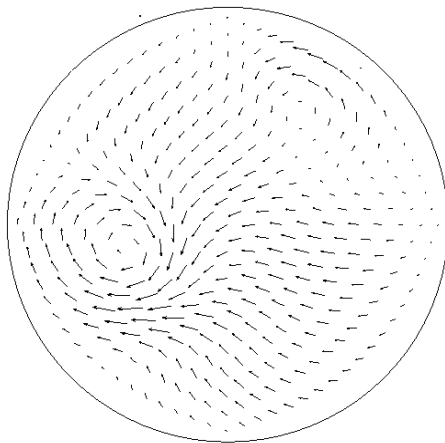
(2) 5 cm/s;

(3) 10 cm/s

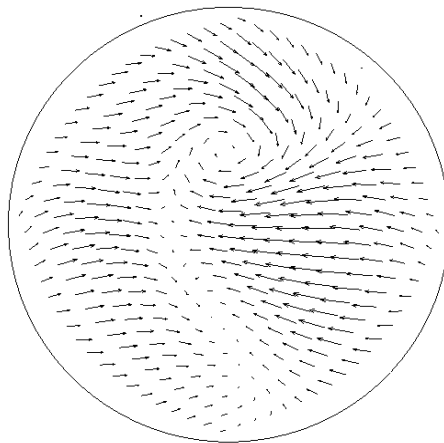
Figure 1.4 The Vector Plot of the Instantaneous Liquid Velocity Projected on a r-z Plane Slice through the Center of a 44-cm Diameter Column Operated at Different Superficial Gas Velocities



(a) Upper section

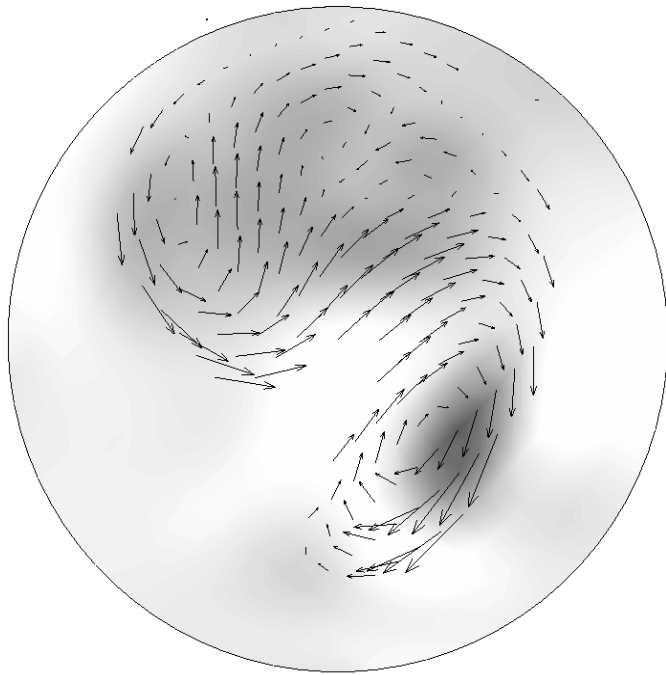


(b) Middle section

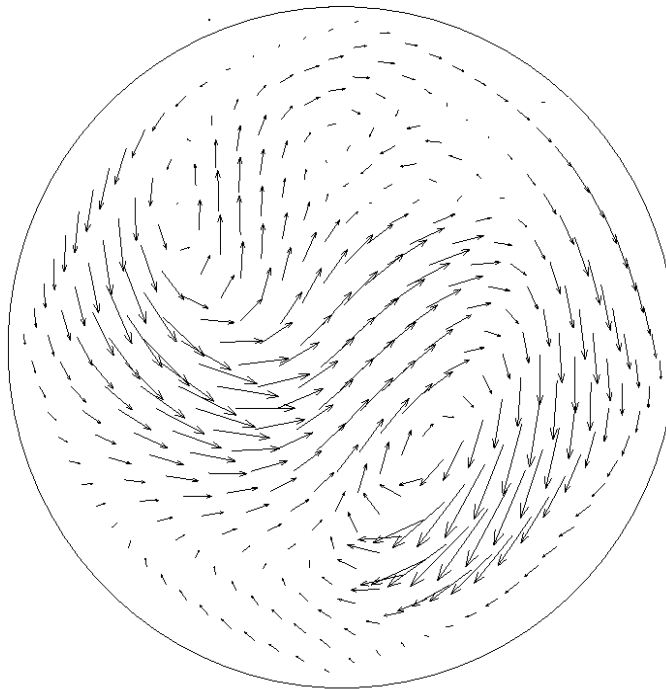


(c) Bottom section

Figure 1.5 The Vector Plots of the Instantaneous Liquid Velocity Projected on Cross-Sectional (x-y) Planes of a 44-cm Diameter Column Operated at a Superficial Gas Velocity of 10 cm/s



(a) Gas holdup and liquid velocity



(b) Liquid velocity

Figure 1.6 The Instantaneous Flow Pattern on a Cross-Sectional Plane of a 44-cm Diameter Column Operated at a Superficial Gas Velocity of 10 cm/s

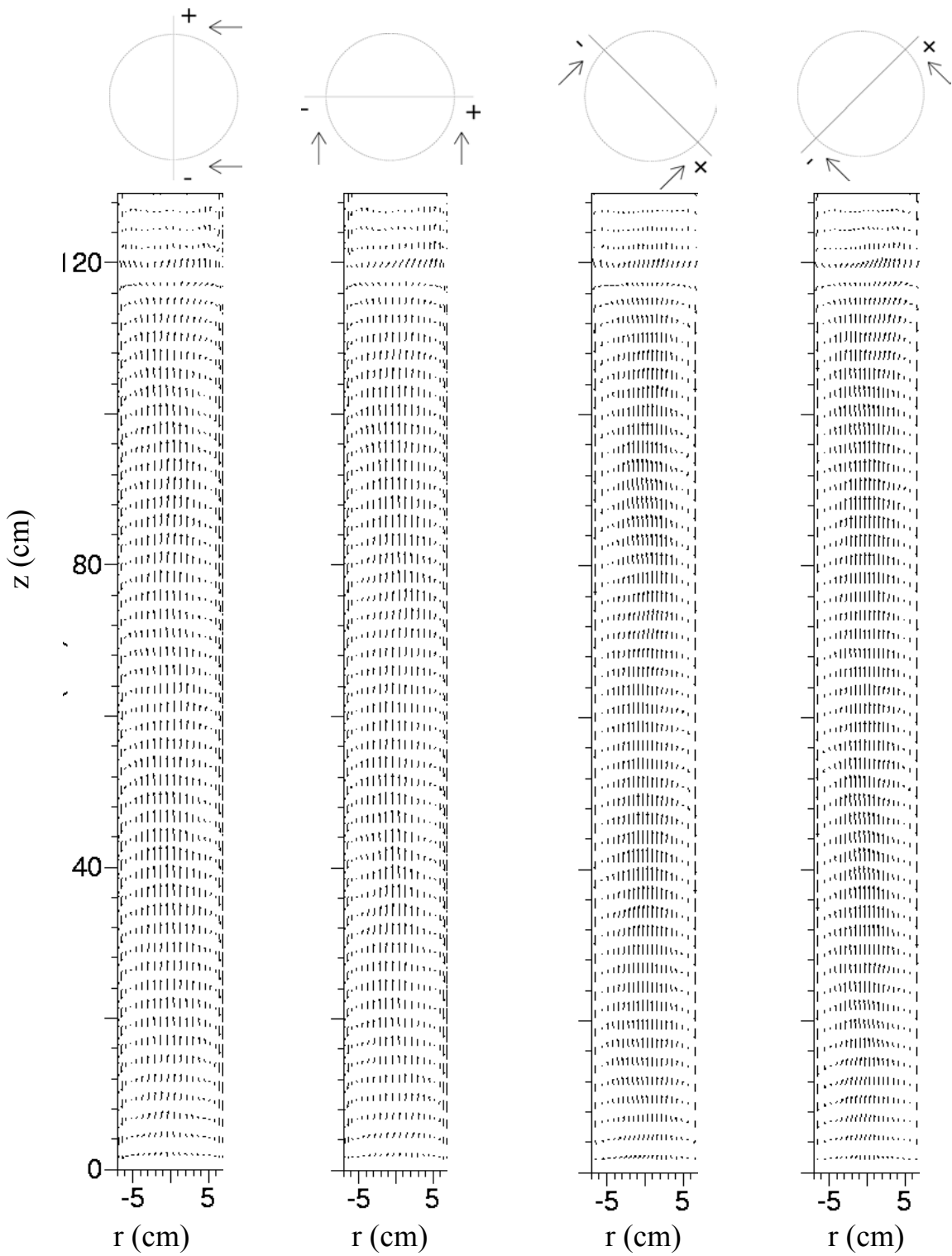
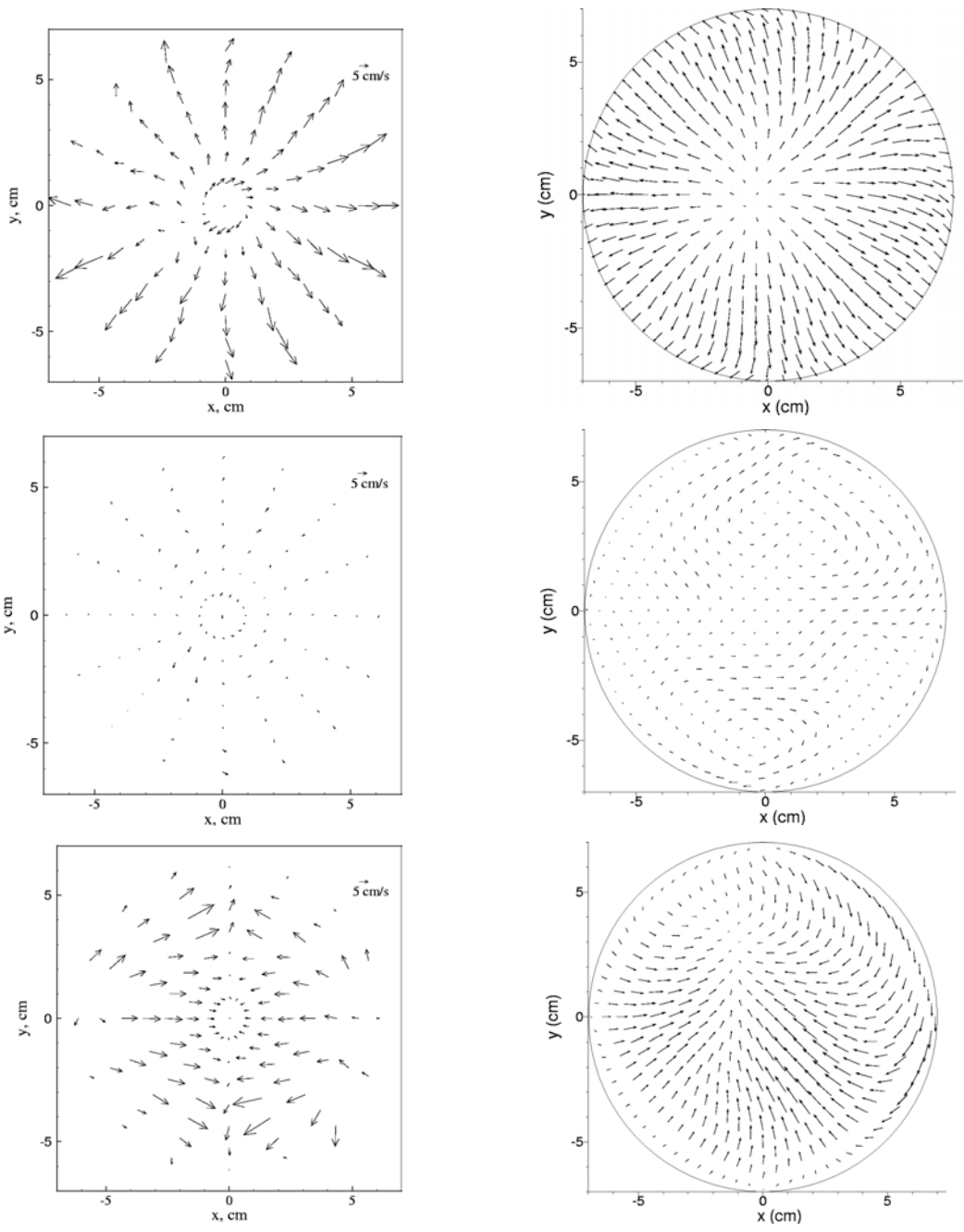


Figure 1.7 Time-Averaged Liquid-Velocity Vectors on Planes Cutting through the Center of the 14-cm Diameter Column Operated at a Superficial Gas Velocity of 4.8 cm/s



CARPT

Simulation

Figure 1.8 Comparison of Time-Averaged Liquid-Velocity Vectors on Cross-Sectional Planes at the Gas Sparger Zone (lower row), the Middle Section (middle row) and the Gas Disengagement Zone (upper row) of a 14-cm Diameter Column at 4.8 cm/s

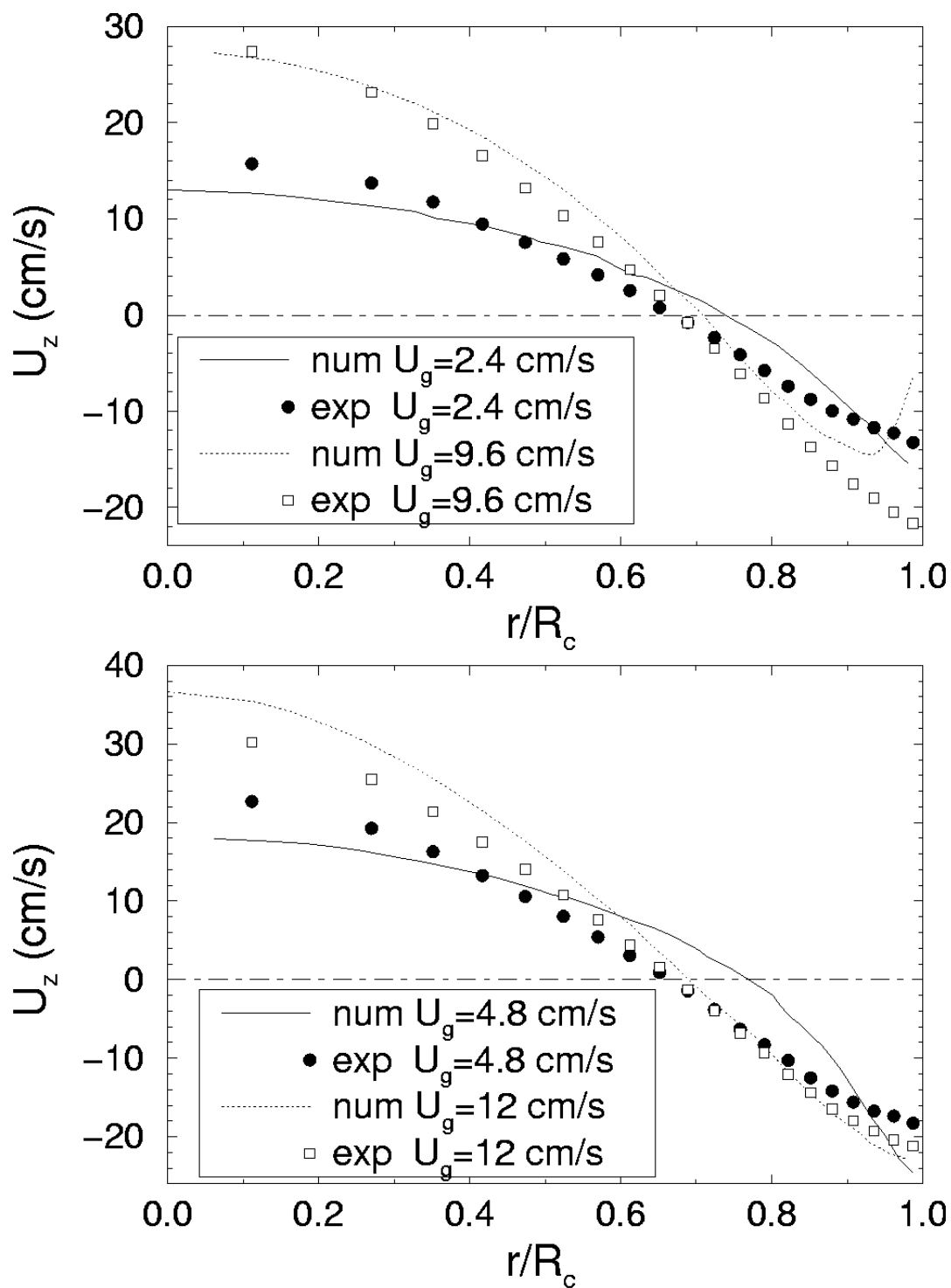


Figure 2.1 Comparison of Radial Profiles of Axial Liquid Velocity obtained from Simulation with Experimental Data measured by the CARPT Technique for a 14-cm Diameter Column

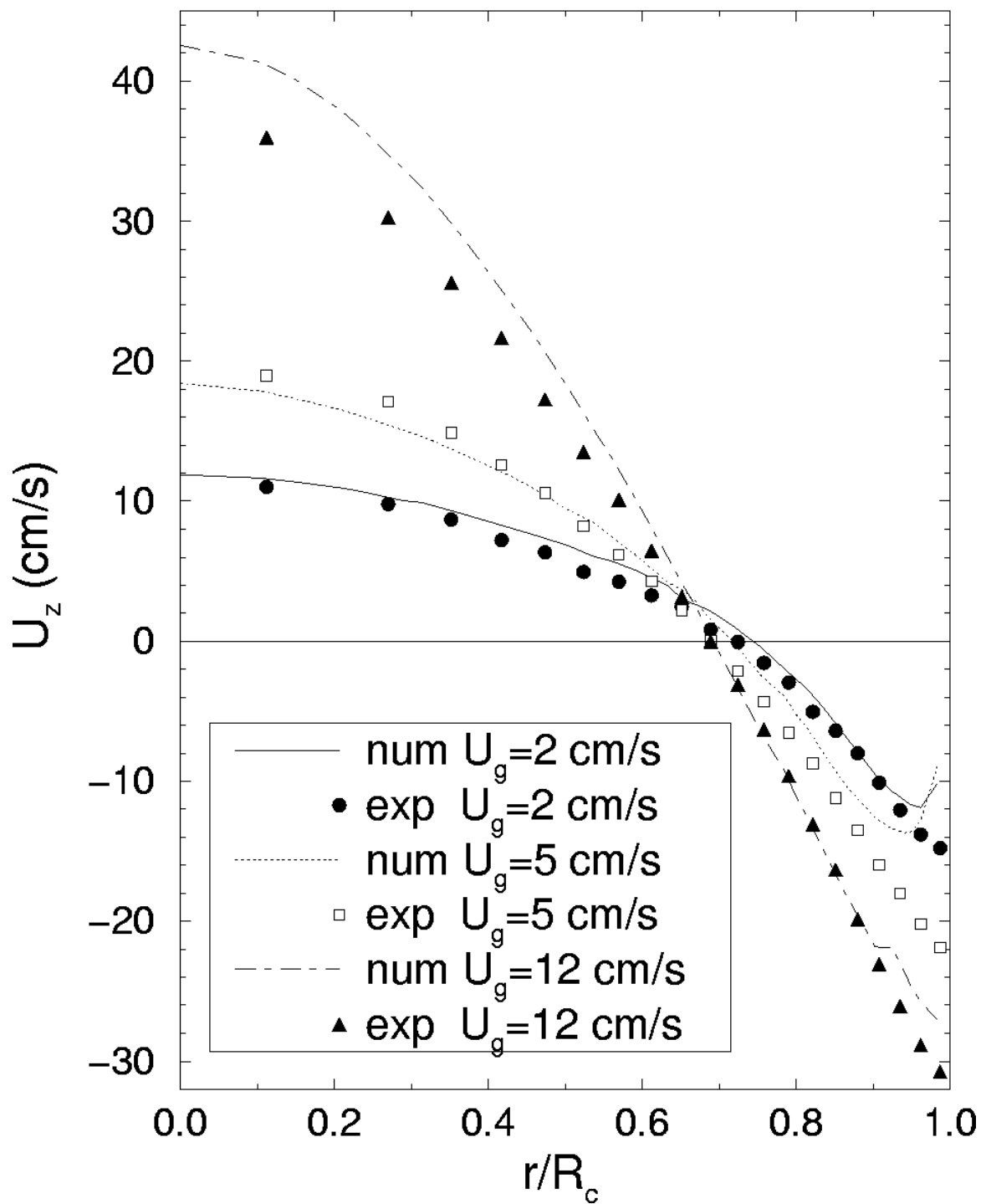


Figure 2.2 Comparison of Radial Profiles of Axial Liquid Velocity obtained from Simulation with Experimental Data measured by the CARPT Technique for a 19-cm Diameter Column

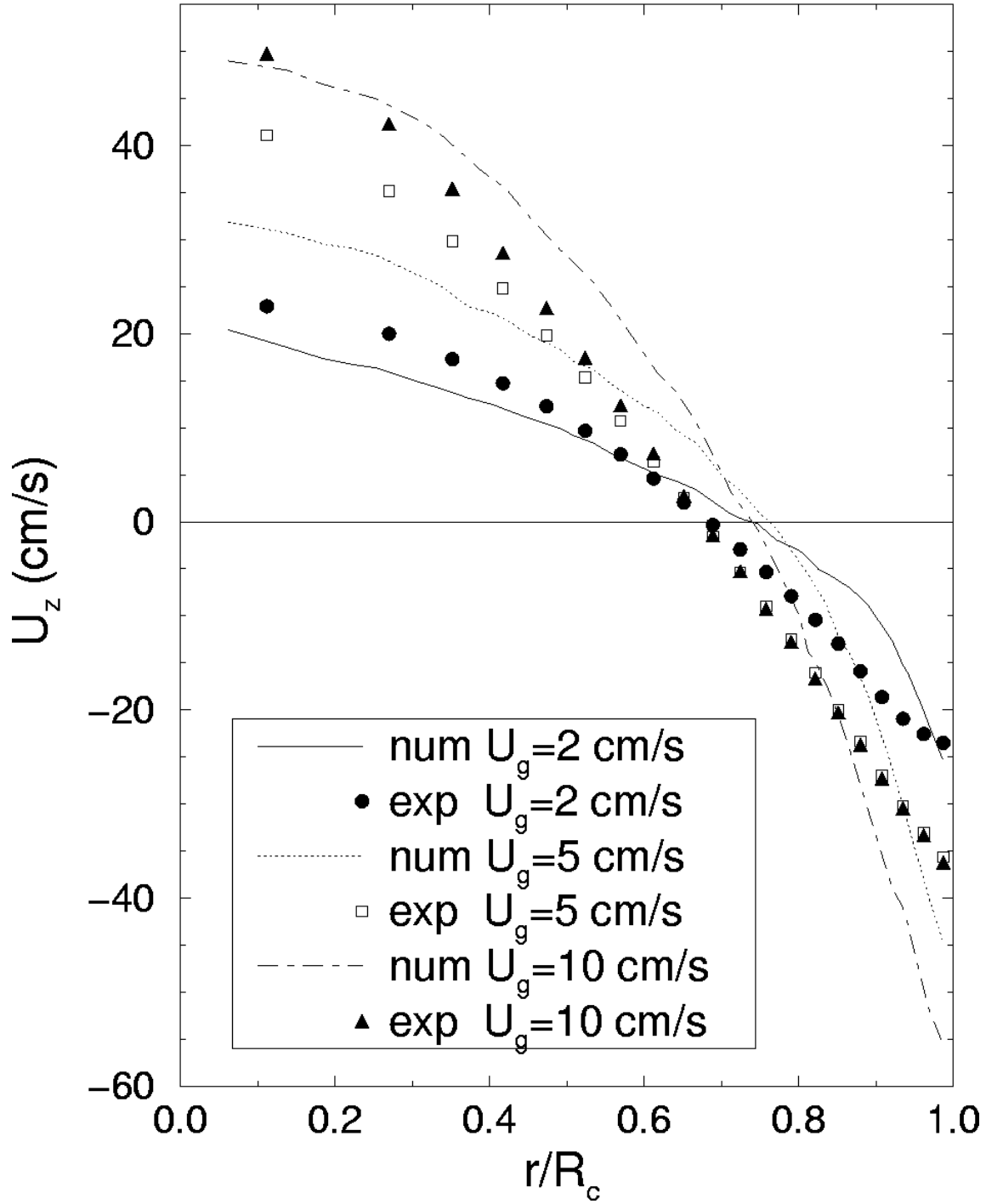


Figure 2.3 Comparison of Radial Profiles of Axial Liquid Velocity obtained from Simulation with Experimental Data measured by the CARPT Technique for a 44-cm Diameter Column

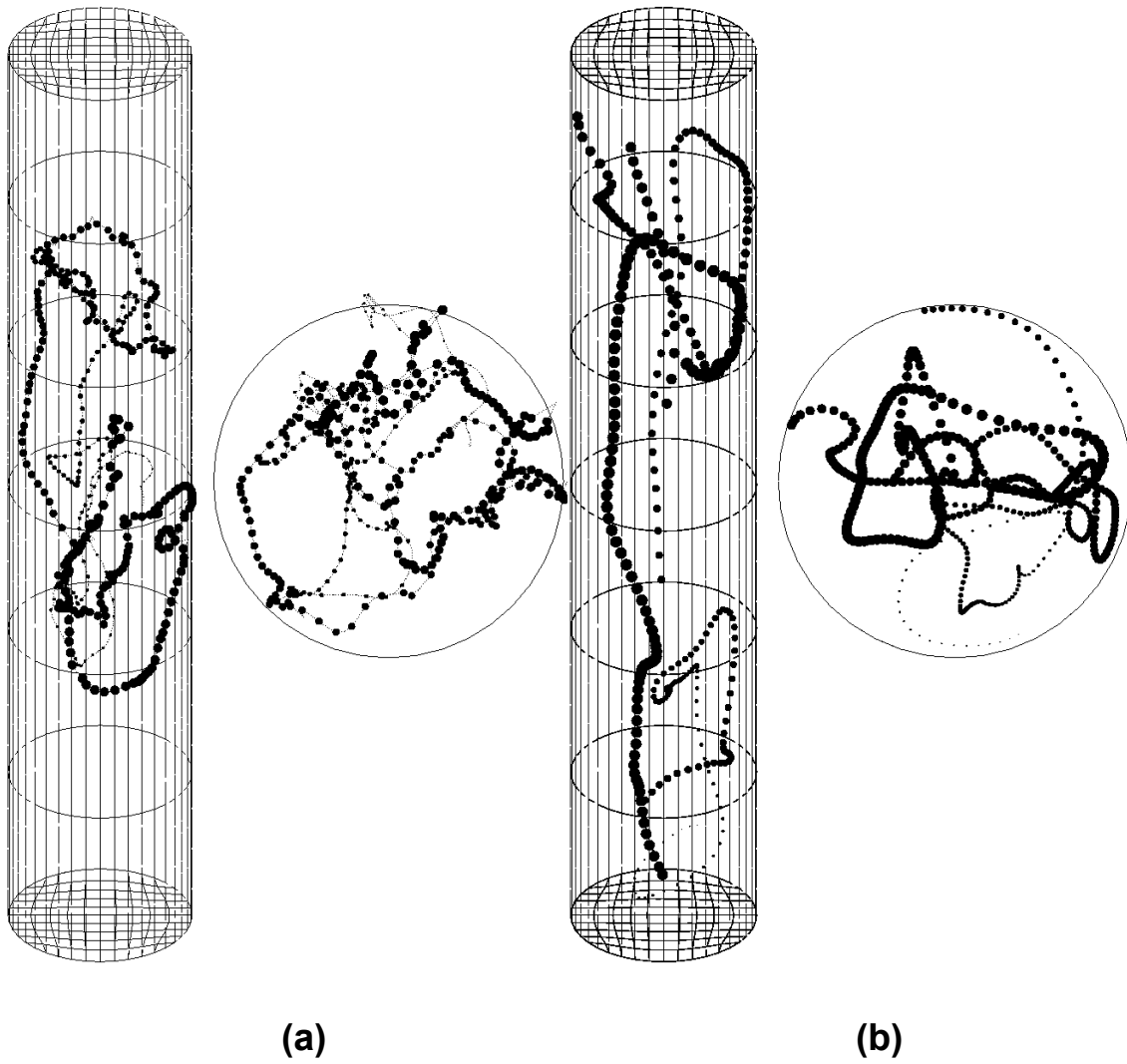


Figure 3.1 The Trajectory of the Tracer Particle in a 44-cm Diameter Column at $U_g=10$ cm/s: (a) CARPT experiment; (b) numerical particle tracking

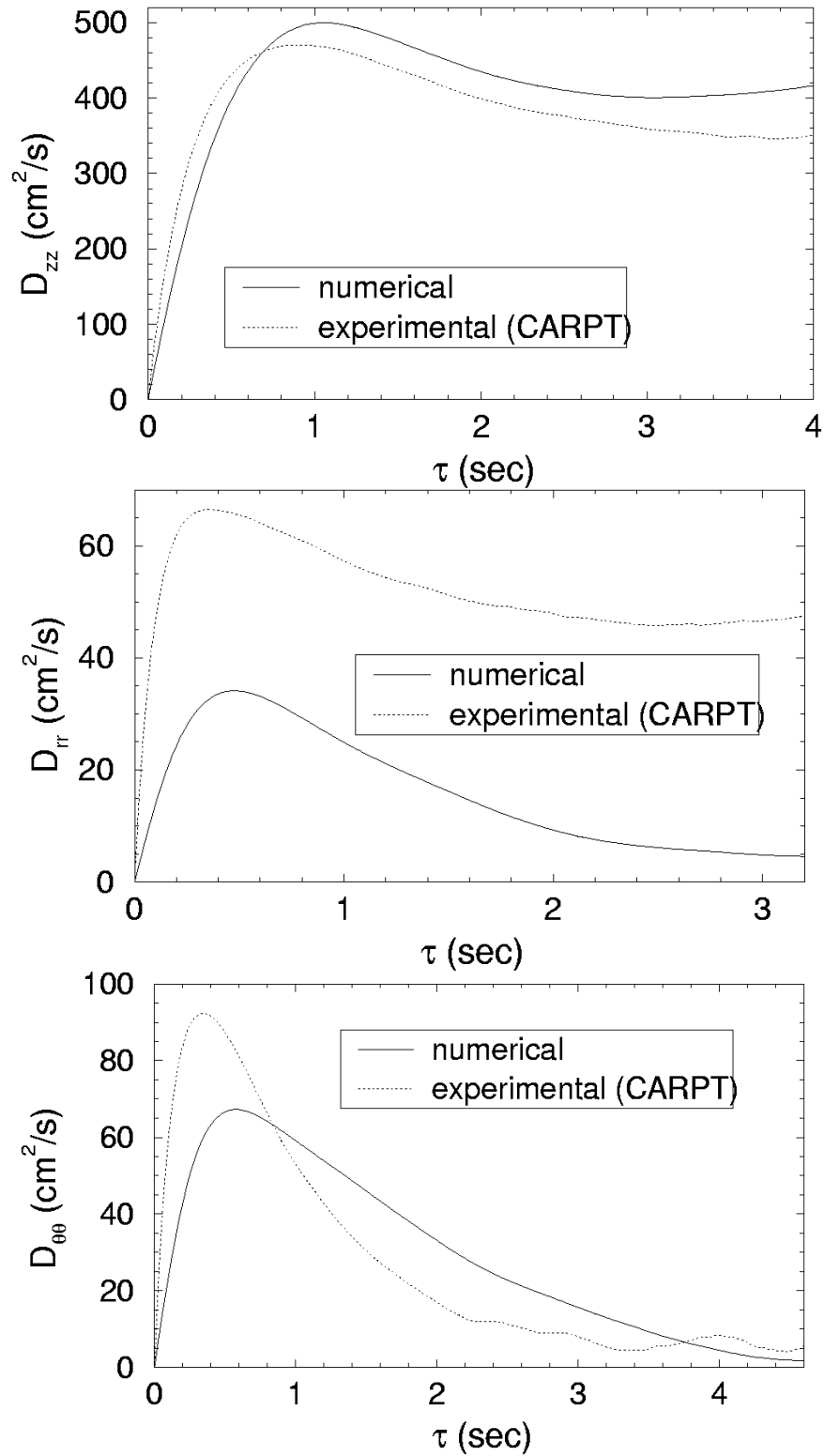


Figure 3.2 The Lagrangian Turbulent Diffusivities in the Middle Section of the 44-cm Diameter Column operated at a Superficial Gas Velocity of $U_g=10$ cm/s

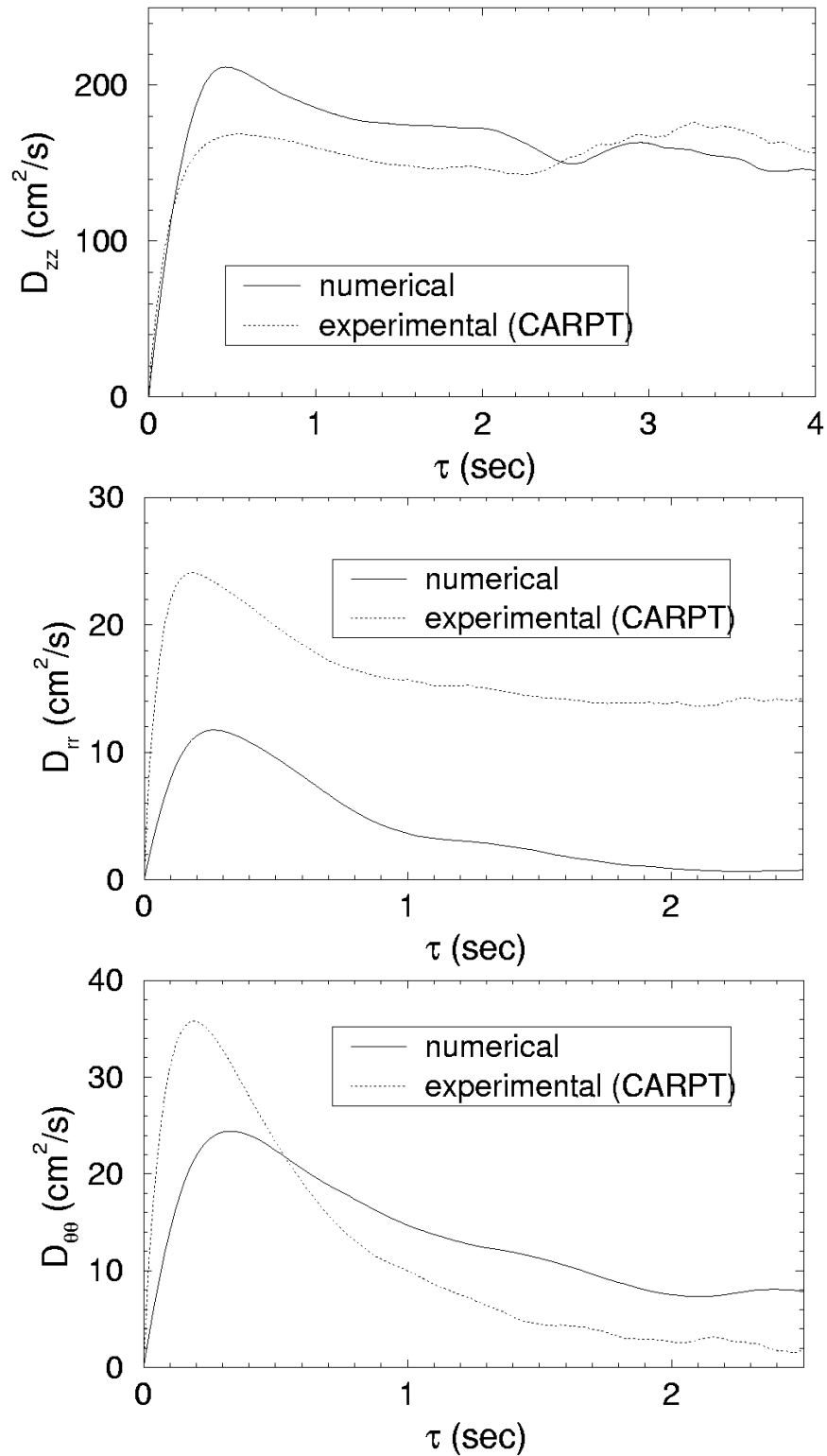


Figure 3.3 The Lagrangian Turbulent Diffusivities in the Middle Section of the 19-cm Diameter Column operated at a Superficial Gas Velocity of $U_g=12$ cm/s